Journal of
Applied Remote Sensing

RemoteSensing.SPIEDigitalLibrary.org

Satellite retrievals of *Karenia brevis* harmful algal blooms in the West Florida shelf using neural networks and impacts of temporal variabilities

Ahmed El-Habashi
Claudia M. Duran
Vincent Lovko
Michelle C. Tomlinson
Richard P. Stumpf
Sam Ahmed

SPIE.

Ahmed El-Habashi, Claudia M. Duran, Vincent Lovko, Michelle C. Tomlinson, Richard P. Stumpf, Sam Ahmed, "Satellite retrievals of *Karenia brevis* harmful algal blooms in the West Florida shelf using neural networks and impacts of temporal variabilities," *J. Appl. Remote Sens.* **11**(3), 032408 (2017), doi: 10.1117/1.JRS.11.032408.

Satellite retrievals of *Karenia brevis* harmful algal blooms in the West Florida shelf using neural networks and impacts of temporal variabilities

Ahmed El-Habashi,[a] Claudia M. Duran,[a] Vincent Lovko,[b] Michelle C. Tomlinson,[c] Richard P. Stumpf,[c] and Sam Ahmed[a,*]

[a]The City College of New York, NOAA CREST, Optical Remote Sensing Laboratory, Department of Electrical Engineering, New York, New York, United States

[b]Mote Marine Laboratories, Sarasota, Florida, United States

[c]National Oceanic and Atmospheric Administration, National Centers for Coastal Ocean Science, Silver Spring, Maryland, United States

Abstract. We apply a neural network (NN) technique to detect/track *Karenia brevis* harmful algal blooms (*KB* HABs) plaguing West Florida shelf (WFS) coasts from Visible-Infrared Imaging Radiometer Suite (VIIRS) satellite observations. Previously *KB* HABs detection primarily relied on the Moderate Resolution Imaging Spectroradiometer Aqua (MODIS-A) satellite, depending on its remote sensing reflectance signal at the 678-nm chlorophyll fluorescence band (Rrs678) needed for normalized fluorescence height and related red band difference retrieval algorithms. VIIRS, MODIS-A's successor, does not have a 678-nm channel. Instead, our NN uses Rrs at 486-, 551-, and 671-nm VIIRS channels to retrieve phytoplankton absorption at 443 nm (a_{ph443}). The retrieved a_{ph443} images are next filtered by applying limits, defined by (i) low Rrs551-nm backscatter and (ii) a minimum a_{ph443} value associated with *KB* HABs. The filtered residual images are then converted to show chlorophyll-*a* concentrations [Chl*a*] and *KB* cell counts. VIIRS retrievals using our NN and five other retrieval algorithms were compared and evaluated against numerous *in situ* measurements made over the four-year 2012 to 2016 period, for which VIIRS data are available. These comparisons confirm the viability and higher retrieval accuracies of the NN technique, when combined with the filtering constraints, for effective detection of *KB* HABs. Analysis of these results as well as sequential satellite observations and recent field measurements underline the importance of short-term temporal variabilities on retrieval accuracies. [DOI: 10.1117/1.JRS.11.032408]

Keywords: neural networks; harmful algal blooms; ocean color remote sensing reflectance; *Karenia brevis*; retrieved chlorophyll-*a*; normalized fluorescence height; West Florida shelf.

Paper 16918SS received Nov. 30, 2016; accepted for publication Apr. 11, 2017; published online May 11, 2017.

1 Introduction

We have previously described preliminary results with a neural network (NN) approach for the detection[1] and tracking of *Karenia brevis* harmful algal blooms (*KB* HABs) that frequently plague the coasts and beaches of the West Florida shelf (WFS) using visible-infrared imaging radiometer suite (VIIRS) satellite data. Such a monitoring capability for *KB* HABs is important because of their negative impacts on ecology and health. More specifically, high *KB* HABs levels pose a threat to fisheries and human health and directly affect tourism and local economies.[2] Effective *KB* HABs detection and tracking approaches are needed for use with VIIRS so that NOAA can extend its HABs monitoring capabilities. These previously relied on MODIS-A

*Address all correspondence to: Sam Ahmed, E-mail: ahmed@ccny.cuny.edu

imagery[3–12] and specifically on the remote sensing reflectance signal at 678 nm, (Rrs678) at the chlorophyll fluorescence wavelength. This was used in MODIS-A with the normalized fluorescence height (nFLH) and related red band difference (RBD) techniques to effectively help in *KB* HABs retrievals. However, the current VIIRS satellite, unlike its predecessor MODIS-A, does not have a 678-nm channel to detect chlorophyll fluorescence. To overcome the lack of a fluorescence channel on VIIRS, the NN approach bypasses the need for measurements of chlorophyll fluorescence, allowing us to extend *KB* HABs satellite monitoring capabilities in the WFS to VIIRS.

The essence of the approach is the application of a standard multiband NN inversion algorithm, previously developed and reported by us.[13–16] This approach takes VIIRS Rrs measurements at the 486-, 551-, and 671-nm bands (or 488, 555, and 667 nm for MODIS-A) as NN inputs and produces the related inherent optical properties (IOPs) at 443 nm as outputs: namely, the absorption coefficients of phytoplankton (a_{ph443}), dissolved organic matter (a_g), and nonalgal particles (a_{dm}) as well as the particulate backscatter coefficient, (b_{bp}). In this work, it is only the NN output of a_{ph443} with which we are concerned. This is used to generate an a_{ph443} image, which is then converted into an equivalent [Chl*a*] image, using empirical relationships for specific chlorophyll absorption values in the WFS, which have been determined from *in situ* measurements.[17] Next, to obtain *KB* values from the VIIRS NN retrieved a_{ph443} image, we apply two filter processes, based on constraints known to be associated with *KB* HABS in the WFS. These constraints are: (i) low backscatter at 551 nm, manifested as a maximum permissible value of Rrs551 $\leq$ Rrs551 max and (ii) a minimum permissible [Chl*a*]min threshold value[9,18,19] and hence an equivalent minimum permissible value: $a_{\text{ph443}} \leq a_{\text{ph443 min}}$. Following application of these two filter processes, the residual image will now show only a_{ph443} values that are compatible with both criteria for *KB* HABs and are, therefore, representative of *KB* HABs.

VIIRS retrievals of *KB* in the WFS, using our NN and five other retrieval algorithms, are then compared and evaluated for their efficacy against datasets of *in situ* measurements. To have enough data for meaningful analysis, *in situ* data sets that cover the available data from the start of the VIIRS mission in January 2012 to October 2016 were created for these comparisons. The comparisons confirmed the viability and potential of the NN technique, when combined with the filtering constraints devised, for effective detection of *KB* HABs in the WFS. Analysis of results as well as sequential satellite observations and field measurements in the WFS also show the importance of short-term temporal variabilities and underline their impact on retrieval accuracies.

2 Materials and Methods Background

2.1 *Neural Network Algorithm Background*

For the development of our NN algorithm,[1,13,14–16] a synthetic data set of 20,000 IOPs was produced based on the NASA bio-optical marine algorithm data set.[20] These IOPs whose range and variability is well represented in the literature[21–34] were then used as inputs to a four component bio-optical model,[15,24,34] which, in conjunction with a HydroLight-based,[35] parameterized forward model, described in Ref. 32, Lee produced 20,000 sets of Rrs values at 486, 551, and 671 nm (for VIIRS) and 488, 555, and 667 nm for MODIS-A. The NN was trained on 10,000 of these values and tested on a 10,000 synthetic subset as well as on field data to solve the inverse problem[36,37] of retrieving physical variables, including a_{ph443}, from Rrs values at 486, 551, and 671 nm, and at 488, 555, and 667 nm. The algorithm is a standard multiband NN inversion algorithm that takes VIIRS Rrs measurements at the 486-, 551-, and 671-nm bands and MODIS-A measurements at 488-, 555-, and 667-nm bands in the WFS as inputs, and produces as outputs the related IOPs, namely: a_{ph443}, a_g, and a_{dm} as well as b_{bp}, all at 443 nm. (As mentioned in the Sec. 1, it is only the a_{ph443} output of NN that we are concerned with here). Detailed descriptions of the NN are given in Refs. 13–16, and Ref. 1 shows the necessary parameters for implementation of the NN with a MATLAB tool for obtaining satellite retrievals.

2.2 *Development of Criteria for Filters to be Used in Processing VIIRS (and MODIS-A) Retrievals of Rrs551 and [Chla] in the WFS to Obtain Residual Images Depicting* KB *HABs Concentrations*

A brief description is given below of the approach used for devising filtering criteria to apply to VIIRS (and MODIS-A) retrieved images of Rrs551 and a_{ph443} (or [Chl$a$]) in the WFS, to evolve residual images depicting *KB* HABs concentrations. This approach, which is described in detail in Ref. 1, is summarized and updated here. Satellite data are obtained from VIIRS and MODIS-A-sensors as level two data products from NASA's processing stream, available from Ref. 38. Pixels are excluded from processing if they have been flagged for land, cloud, failure in atmospheric correction, stray light, bad navigation quality, both high and moderate glint, negative Rayleigh corrected radiance, and solar zenith larger than 70.

2.2.1 *VIIRS retrievals of Rrs551 and a_{ph443} and determination of limiting values of Rrs551max and a_{ph443} min compatible with* KB *HABs in the WFS*

This section updates and revises an earlier analysis carried out in Ref. 1 to determine limiting values of Rrs551max and a_{ph443} min compatible with *KB* HABs in the WFS. By searching more thoroughly through available data bases, we are able to constrain comparison of VIIRS satellite retrievals on 10/9/12 to *in situ* measurements carried out all on the same day. This constraint provides a much more convincing comparison of satellite retrievals to *in situ* values from which to select our limiting values than was done in Ref. 1. In the latter, available retrievals from VIIRS on one clear day (9/2/14) were compared with *in situ* measurements, not carried out on the same day, but rather over an overlapping 22-day period (8/27/2014 to 9/17/2014) during which conditions could clearly have changed much more substantially.

Figure 1 shows *in situ* measured *KB* cell counts associated with a prominent *KB* HAB bloom in the WFS with its peak occurring on 10/09/2012, from the NOAA HABSOS.[39] This shows the bloom area with indicators (circles of different sizes) for measured *KB* HABs cell counts for that date. We next compare NN retrievals from VIIRS observations to these cell counts. Using Rrs486-, 551-, and 671-nm measurements from VIIRS as inputs to the NN, we retrieve

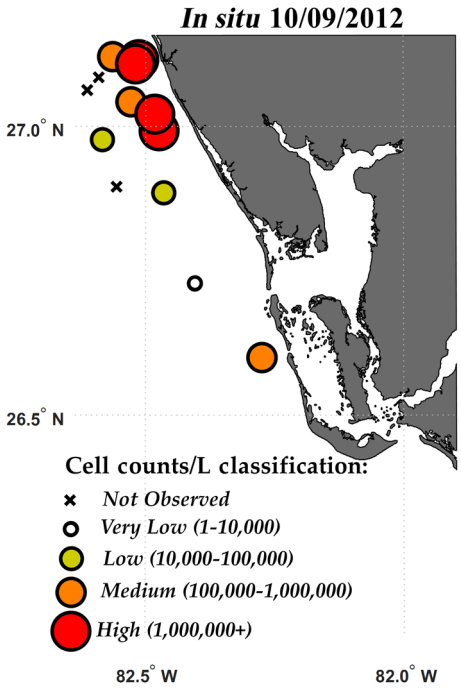

Fig. 1 NOAA HABSOS data[39] with *in situ KB* concentrations for October 9, 2012.

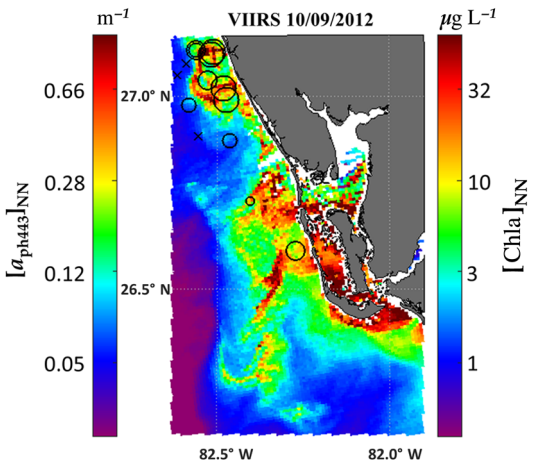

Fig. 2 NN retrieved a_{ph443} (LHS) equivalent [Chl*a*] (RHS).

a_{ph443} for the same date and area shown in Fig. 1. These retrievals are shown in Fig. 2, which also shows on the right-hand scale the equivalent [Chl*a*] converted from a_{ph443} using the empirical relationship of Ref. 17

$$a_{ph443} = 0.051 \times [\text{Chl}a]^{0.74}, \ \text{m}^{-1}. \tag{1}$$

The challenge then remains to retrieve from Fig. 2 only the a_{ph443} or equivalent [Chl*a*] that represents *KB* HABs by filtering out pixel values incompatible with *KB* HABs. To do this, it is necessary to first define and apply the filters, which, as discussed in Sec. 1 and in more detail in Ref. 1, serve to eliminate pixels that have Rrs551 backscatter and a_{ph443} (or [Chl*a*]) values that are incompatible with *KB* HABs. The two filter processes are summarized next.

Considerations of backscatter values coexisting with *KB* Refs. 12, 18, and 19 show maximum permissible values of backscatter, compatible with *KB* HABs, as $b_{bp}550 \leq 0.0045$ m^2 mg^{-1} at 550 nm. Then, if Rrs551 is taken to serve as a proxy for backscatter, the equivalent max permissible value is Rrs551 $\leq 7.0 \times 10^{-3}$ sr^{-1}. However, by inspection of numerous VIIRS retrievals of Rrs551 against more than 100 simultaneous or near simultaneous *in situ* measurements of *KB* HABs occurrences in the WFS over the 2012 to 2016 period (discussed in Sec. 3), we concluded that a value of approximately Rrs551 $\leq 6.0 \times 10^{-3}$ sr^{-1} appears more appropriate as the highest permissible Rrs551 limiting value compatible with the existence of *KB* HABs. So that would define the limits of the first processing filter, hereinafter denoted as F1, which when applied to VIIRS retrievals of Rrs551, would be used to eliminate pixels with higher values, as being incompatible with the existence of *KB* HAB blooms. The application of this filter process F1 is described in the next section.

2.2.2 *Backscatter limiting values compatible with* KB *HABS and filter process F1*

Figure 3(a) shows VIIRS retrievals of Rrs551 for the same *KB* HABs peak date 10/9/2012 and location. When filter process F1 is applied to Fig. 3(a), all pixels with $Rrs551 \geq 6.0 \times 10^{-3} sr^{-1}$ are screened out, leaving the residual pixels in Fig. 3(b) as a mask retaining only pixels compatible with *KB* HABs as far as backscatter is concerned.

We next apply this pixel mask, from Fig. 3(b), to the VIIRS NN retrieved a_{ph443} for the same October 9, 2012, date and location, and shown in Fig. 2. Eliminating pixels outside the mask area, results in eliminating all a_{ph443} values in Fig. 2 that do not satisfy the Rrs551 $\leq 6.0 \times 10^{-3}$ sr^{-1} requirements for compatibility with *KB* HABs. Residual a_{ph443} values, resulting from this F1 filter process, and, shown in Fig. 3(c) now satisfy the Rrs551 limit requirements for compatibility with *KB* HABs.

2.2.3 *Filter process F2 to apply limits to NN retrieved a_{ph443} (or equivalent [Chla]) images to obtain residual images with values compatible with and depicting* KB *HABs concentrations*

We next consider the appropriate F2 filter values for retaining only a_{ph443} values that were in the F1 filtered image, Fig. 3(c), that are compatible with *KB* HABs. Refs. 18 and 19 show the minimum [Chl*a*] concentration compatible with *KB* HABs in the WFS as $[\text{Chl}a] \geq 1.5\ \mu\text{g} \cdot \text{L}^{-1}$. This is converted into equivalent a_{ph443} using the empirical relationship[17]which gives $a_{\text{ph443}} \geq 0.0688\ \text{m}^{-3}$ as the minimum permissible value. However, by inspection of VIIRS NN retrieved a_{ph443} values against more than 100 *in situ* measurements of *KB* HABs cell values in the WFS over the 2012 to 2016 period (see discussion in Sec. 3) we find that a value of approximately $a_{\text{ph443}} \geq 0.061\ \text{m}^{-3}$ or equivalent [Chl*a*] is more appropriate as the limiting values of a_{ph443} and [Chl*a*] for compatibility with *KB* HABs.

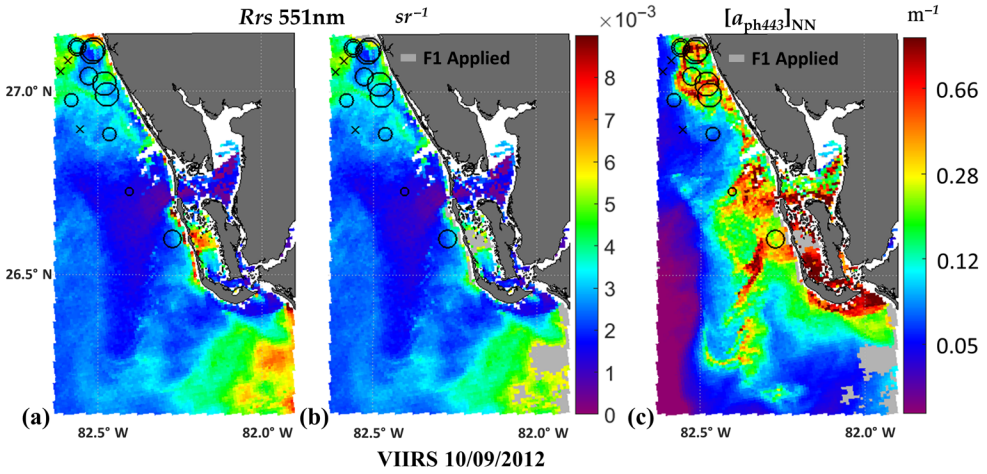

Fig. 3 (a) VIIRS Rrs551 image; (b) residual Rrs551 image after F1 mask (light gray) is applied showing residual ($\text{Rrs551} \leq 0.006\ \text{sr}^{-1}$). Note that these images are overlaid with NOAA-HABSOS *KB* cell counts, from Fig. 1. (c) Residual image after filter F1 is applied to Fig. 2 retrievals. White areas represent cloud cover or invalid data.

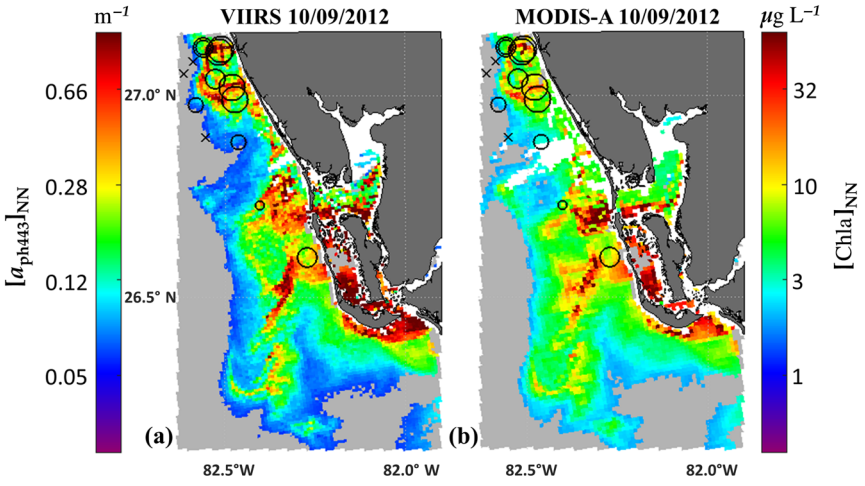

Fig. 4 (a) VIIRS retrieved NN a_{ph443} (left-hand scale) and equiv. [Chl*a*] (right-hand scale) after filter process masks F1 and F2 are applied. These residual values are, therefore, compatible with and show the extent of the *KB* blooms; (b) MODIS-A NN retrieved a_{ph443} (left-hand scale) and equiv. [Chl*a*] (right-hand scale) after filter process masks F1 and F2 are applied. Residual values are, therefore, compatible with and indicate *KB* blooms. Light gray represents F1 and F2 masks and white represents cloud cover or invalid data.

Applying this value as filter F2 to Fig. 3(c), we eliminate pixels that are not compatible with *KB* and end up with the residual Fig. 4(a). This shows only residual values with $a_{ph443} \geq 0.061$ m^{-3} which at the same time satisfy the backscatter F1 filter requirement Rrs551 $< 6.0 \times 10^{-3}$ sr^{-1}. These are, therefore, residual values satisfying both F1 and F2 filter requirements and are, therefore, compatible with and representative of *KB* HABs. Comparison of the residual a_{ph443} (left-hand scale) and equivalent [Chl*a*] (right-hand scale) in Fig. 4(a), which represents the retrieved *KB* HABs values, with the overlaid cell count information from Fig. 1, shows good qualitative agreement. Figure 4(b) shows the equivalent NN a_{ph443} from MODIS-A for the same date and location, and also filtered for the same Rrs551 backscatter and a_{ph443} compatibility requirements (but using the equivalent 488-, 555-, and 667-nm bands of MODIS-A as inputs to the NN instead of the VIIRS bands). Again, we see good qualitative agreement with the *in situ* values of Fig. 1.

2.2.4 *Rrs spectra associated with* KB *HAB blooms*

We next examine the relationship between VIIRS Rrs multiwavelength spectra and the different concentrations of *in situ KB* HABs reflected in the wide variety of [Chl*a*] values of Fig. 4(a) for the bloom of 10/09/2012. Figure 5(a) shows Rrs reflectance spectra observed for low bloom concentration locations. It is color-coded to reflect the measured *in situ* concentrations at these locations. Figure 5(b) shows the Rrs spectra for medium and high bloom locations. As can be seen, both the magnitude and shape of these reflectance spectra change with varying underlying *in situ* bloom concentrations. Thus, with increasing cell concentration, the increased absorption is seen to dominate over the low backscatter associated with *KB* cells, so that magnitudes of Rrs decrease as bloom concentrations increase. Furthermore, for higher bloom concentration, this combination of absorption and low backscatter features results in a decrease in

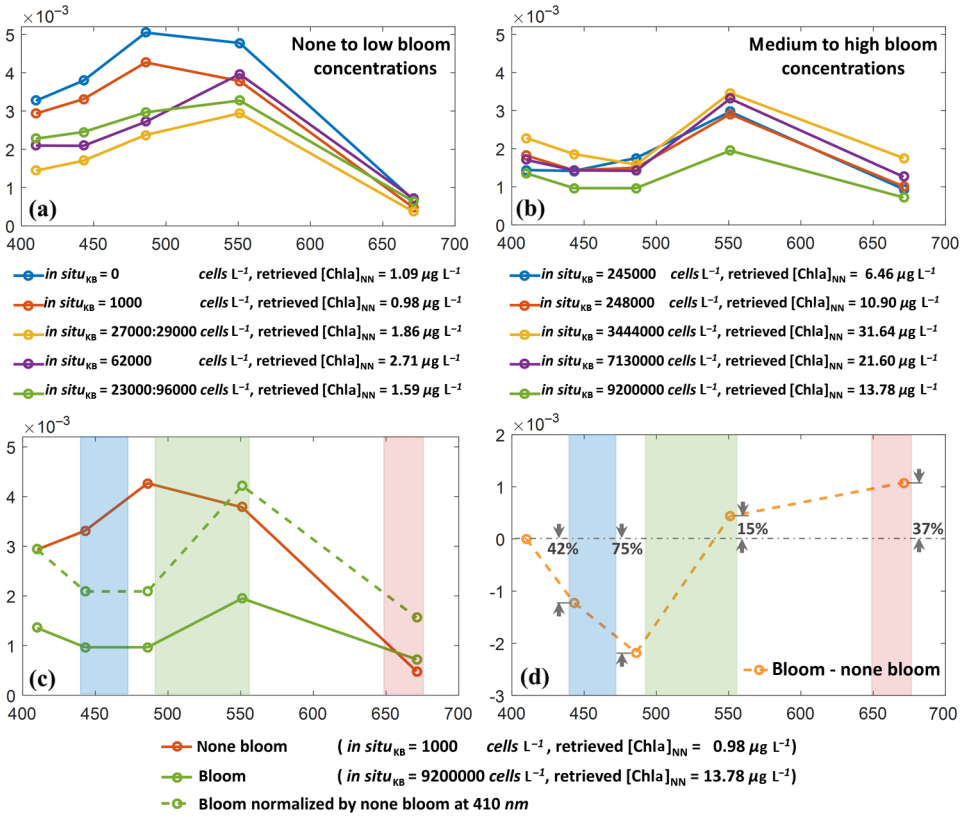

Fig. 5 Matchup of VIIRS Rrs reflectance spectra on 10/09/2012 for: (a) low *in situ* cell count locations. (b) Medium cell to high counts locations; (c) very low bloom Rrs (orange), high bloom Rrs (green) and high bloom Rrs normalized to low bloom Rrs value at 410 nm (dashed green). (d) Differences between low and normalized high bloom.

the blue part of the spectrum with respect to the green. The features, shown below, retrieved from satellite observations, have also been previously observed with *in situ* measurements of *KB* HABS.[18]

The change in spectral shape is brought out in Fig. 5(c), in which the Rrs spectrum for a high bloom concentration (green) is normalized to the reflectance spectra (orange) at 410 nm, of very low *KB* (i.e., low [Chl*a*] shown dotted in red). The difference between the two spectra (high and low bloom or [Chl*a*]) is shown in Fig. 5(d), whose shape exhibiting with the decrease in green reflectance relative to the blue and red helps provide confirmation that we are dealing with *KB* HABs of increasing intensity.

3 Evaluation of VIIRS *KB* HABs Retrievals, Obtained Using NN and Other Algorithms, against *In Situ* Measurement for Matchups Occurring over 2012 to 2016 Period

We next examine VIIRS NN retrievals of *KB* HABs in the WFS, using the limiting F1 and F2 filter approach described in Sec. 2, against coincident, or near coincident, *in situ* measurements. We also compare these VIIRS NN retrievals and *in situ* matchups against retrievals and matchups obtained using other direct retrieval algorithms. In doing so, it is not the intention to present an exhaustive comparison of the many approaches that have been studied for the detection of *KB* HABs in the WFS. Some of these are listed in Refs. 3–12. For more details, the reader is referred to recent excellent surveys and comparisons in Refs. 4–12. Rather, we focus on techniques that have the potential to retrieve images from VIIRS observations that will show concentration and distribution of *KB* HABs at the time of observation. Below, we briefly summarize the main retrieval techniques that might be used for *KB* HABs retrievals.

3.1 *Existing and Potential* KB *HABs Algorithms to be Considered for VIIRS Retrievals*

Existing or potential satellite algorithms that are relevant to the detection of *KB* HABs in the WFS rely on retrieved chlorophyll-*a* concentrations [Chl*a*] as part of their processing. They fall primarily into three categories: (i) using the remote sensing reflectance fluorescence signal at Rrs678 measured by the MODIS-A satellite; (ii) using blue-green ratio algorithms, obtained from the NASA OC3/OCI[20,40–42] and include the chlorophyll-*a* anomaly technique and related approaches;[43–53] and (iii) [Chl*a*] retrievals that are obtained from NASA products, including generalized inherent optical property (GIOP) and quasi-analytical algorithm (QAA) (see below for definitions), and a more recent WFS region specific empirical algorithm, the red green chlorophyll-*a* index (RGCI) which retrieves [Chl*a*] using two visible VIIRS or MODIS-A bands.[54]

Those methods using the 678-nm fluorescence signal include: (a) the nFLH, where FLH is a measure of the solar stimulated chlorophyll-*a* fluorescence, obtained from water leaving radiance Lw (λ). Normalized nFLH[3–12,55–57] is obtained from water leaving radiances normalized to the down-welling light at the sea surface; nFLH is in turn computed as the difference between the observed normalized water leaving radiance [nLw(678)] and a linearly interpolated nLw(678) from the two surrounding bands; (b) the RBD techniques; and (c) the *KB* bloom index (*KB*BI).[4,5] While these techniques, or a combination of them, have generally exhibited good retrieval statistics,[9,12] they are, unfortunately, not applicable to VIIRS, the successor satellite, which unlike its predecessor, MODIS-A does not have a 678-nm fluorescence channel. Since, in this paper, we are concerned only with retrieval techniques applicable to VIIRS, fluorescence techniques are not included in any further discussions.

In the following sections, we focus on comparing VIIRS [Chl*a*] retrievals against coincident or near coincident *in situ* measurements of *KB* cell counts and their equivalent [Chl*a*]. In prior work,[1] we analyzed satellite retrievals against *in situ* measurements, in which NN VIIRS retrievals were compared against retrievals using OCI/OC3 (Refs. 42 and 43) and RGCI.[54] In this paper, we have now added comparisons of NN retrievals with those using the GIOP[58–60] and QAA[61,62] widely used algorithms. This remedies an important omission in our previous publication[1] and

extends NN retrieval comparisons to include comparisons with all available VIIRS direct retrieval techniques. Thus, algorithms compared with NN now include GIOP and QAA, as well as OCI/OC3, and RGCI for new overlap time windows (see Secs. 3.2 and 3.3). The salient features of these different NASA retrieval algorithms are summarized below.

The OCI/OC3 indexes, both NASA products,[43] use [Chl*a*] retrieval algorithms that make use of the ratio of blue/green bands in the MODIS-A and VIIRS satellites[20,40–43] and were found to yield exactly the same retrievals for our WFS conditions.

GIOP model. While there are numerous semianalytical algorithms (SAAs) existing to estimate IOPs, GIOP allows construction, evaluation, and selection of specific modeling assumptions from different SAAs at runtime, in order to generate a unified IOP model. This NASA algorithm[58–60] returns spectral marine absorption and backscattering coefficients for water column constituents [e.g., colored dissolved organic material and algal and nonalgal particles] in m^{-1}, calculated using the default global configuration of the GIOP model. We use it here to retrieve [Chl*a*] from VIIRS observations for matchups with *in situ* measurements.

Quasi-analytical algorithm version 5 (QAA_5)[61,62] developed by Lee et al. to derive the absorption and backscattering coefficients by analytically inverting the spectral remote-sensing reflectance [Rrs(λ)]. It starts with an empirical estimate of the total absorption coefficient at a reference wavelength (550, 555, or 560) and then analytically calculates the backscattering coefficient at the same wavelength. The amplitude of these coefficients at other wavelengths is obtained using an empirical estimate of the particulate backscattering spectral shape and the measured remote-sensing reflectance. After the total absorption coefficient is known, it can be further decomposed into the algal and nonalgal components. We use it here to retrieve [Chl*a*] from VIIRS observations for matchups with *in situ* measurements.

RGCI is an empirical WFS region specific retrieval algorithm[54] that retrieves [Chl*a*] from observations of MODIS-A and VIIRS bands. For VIIRS, the [Chl*a*] retrievals are given by

$$[\mathrm{Chl}a]_{\mathrm{RGCI}} = 0.1 \times \exp\left(11.8 \times \frac{\mathrm{Rrs671}}{\mathrm{Rrs551}}\right),\ \mu\mathrm{g\,L^{-1}}. \tag{2}$$

The above algorithms, all applicable with VIIRS, will be used for retrieval comparisons against *in situ* measurements and comparisons against VIIRS NN.

3.2 *Available Matchups for VIIRS Observations of the WFS Over the 2012 to 2016 Period*

The ultimate test for the viability of *KB* HABs satellite retrieval techniques is their ability to match retrieved values with concurrent *in situ* measurements. However, it is difficult on any one day to find sufficient matchups between satellite observations and concurrent, or near concurrent, *in situ* measurements to obtain statistically meaningful results. We, therefore, extended the study period to look at all available WFS matchups, Fig. 6, between VIIRS measurements and *in situ* data at concurrent dates and over the 2012 to 2016 period for which there was available VIIRS data.

We then looked for matchups where the overlap time windows between satellite observations and *in situ* measurements were 15 and 100 min.

It was found that there were 36 matchups of available *in situ* measurements that satisfy the matchup conditions for satellite observations within a 15-min overlap time window, including those pixels that show *KB* cell concentrations at values below those considered to be officially labeled as blooms. The additional conditions stipulated for matchup were that pixel centers were: 0.3 miles or less from the *in situ* measurement location. This represents an empirical approach to ensure that pixel values could be reasonably assumed to reflect the related *in situ* measurements and hence reduce potential impact of patchiness[63] within the pixel ($\sim$0.7 km^2 for VIIRS and $\sim$1 km^2 for MODIS). Pixels were also excluded from the matchup comparison if they had been flagged for land, cloud, failure in atmospheric correction, stray light, bad navigation quality, both high and moderate glint, negative Rayleigh corrected radiance, and solar zenith larger than 70 deg, and any pixels that had water leaving radiance spectra with negative values in any one of its wavelengths. Cell count sample measurements also had to be at less than 1 m depth and

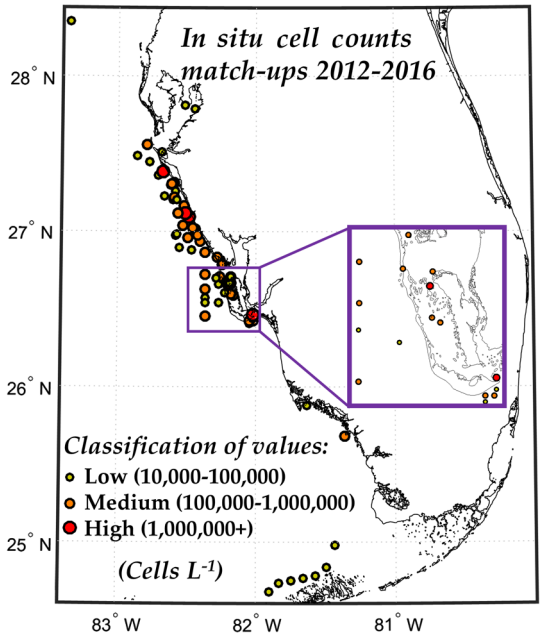

Fig. 6 Showing *in situ* locations of *Karenia brevis* cell counts cover the range 0.01 to 9.2×10^6 cells $\cdot$ L^{-1} obtained from Florida Fish and Wildlife Conservation Commission (FWC). Zoomed area illustrates the extent of the underline details of *KB* values available in VIIRS retrievals for the period of 2012 to 2016.

Table 1 Seasonal distribution of matchups used in the comparison of retrieval accuracies.

January 2012 to March 2016	Winter	Spring	Summer	Fall	Total
Number of matchups	18	6	1	68	93

at concentrations $\geq 10^4$ cells $\cdot$ L^{-1}. It should be noted[47] that [Chl*a*] of 1 μg $\cdot$ L^{-1} is taken as $\sim 10^5$ cells $\cdot$ L^{-1}. The *in situ* cell count data were obtained from the Florida Fish and Wildlife Conservation Commission's Fish and Wildlife Research Institute (FWC-FWRI). The search for matchup between VIIRS satellite and *in situ* observations on the same day and within a 100-min window of the overpass time showed 93 cases that satisfied the matchup conditions as specified above. The seasonal distribution of these 93 matchups between satellite observations and *in situ* measurements used in the comparison of retrieval accuracies is shown in Table 1.

3.3 *Comparisons of VIIRS Retrievals Using NN and Other Algorithms Against* KB *HABs In Situ Measurements in the WFS Over the 2012 to 2016 Period for 100- and 15-min Windows between the Overpass Time and In Situ Observations*

We next revise the comparisons of NN retrieval accuracies from comparisons with OCI/OC3 and RGCI in Ref. 1 to (i) reflect different matchup overlap time windows with *in situ* measurements and (ii) also extend them to now include comparisons with GIOP and QAA. The change in time windows is also a significant change from Ref. 1. Thus, the matchup overlap time windows between retrievals and *in situ* measurements for the statistical comparison of NN retrievals with other techniques were changed to 100 and 15 min in this paper, from the previous time windows of: daily, 60, and 30 min in Ref. 1. The daily matchup was eliminated as being too inaccurate.

The 100-min time window conforms to the approximate time between consecutive overpasses of the VIIRS satellite and consecutively retrieved images, which can also provide evidence of the temporal variations observed with *KB* HAB blooms. These are the subject of Sec. 3.5. The shorter 15-min time window was selected after an investigation for this paper found 15 min to be the shortest time window, which at the same time provided enough matchup points for meaningful statistical analysis. This approach is borne out by the results that show much better matchups for the 15-min window. This has important implications regarding the validity of satellite observations of *KB* HABs.

The relationship between retrieved [Chl*a*] using the NN, OCI/OC3, and RGCI algorithms and the *in situ KB* cell count measurements for the 100- and 15-min matchup time windows are shown in Fig. 7. For NN, OCI/OC3, and RGCI retrievals, it was found that there were 93 valid observations within the 100-min window between overpass time and the *in situ* measurements. In these results, R^2 is the coefficient of determination. To determine R^2, the orthogonal linear regression approach (OR) was used where errors are assumed to exist for both variables. The error (ε) is calculated as the sum of orthogonal distances. OR estimates of X on Y will minimize the orthogonal distance from the observed data points to the regression line[64]

$$\sum (y_i - \beta_0 - \beta_1 x_i)^2, \tag{3}$$

where β_0 and β_1 are intercept and slope and the OR estimate of the slope is

$$\widehat{\beta_1} = \frac{S_{YY} - S_{XX} + \sqrt{(S_{YY} - S_{XX})^2 + 4S_{XY}^2}}{2S_{XY}}, \tag{4}$$

where S_{XX} and S_{YY} are the covariance for X and Y, respectively, and S_{XY} is the correlation for X and Y.

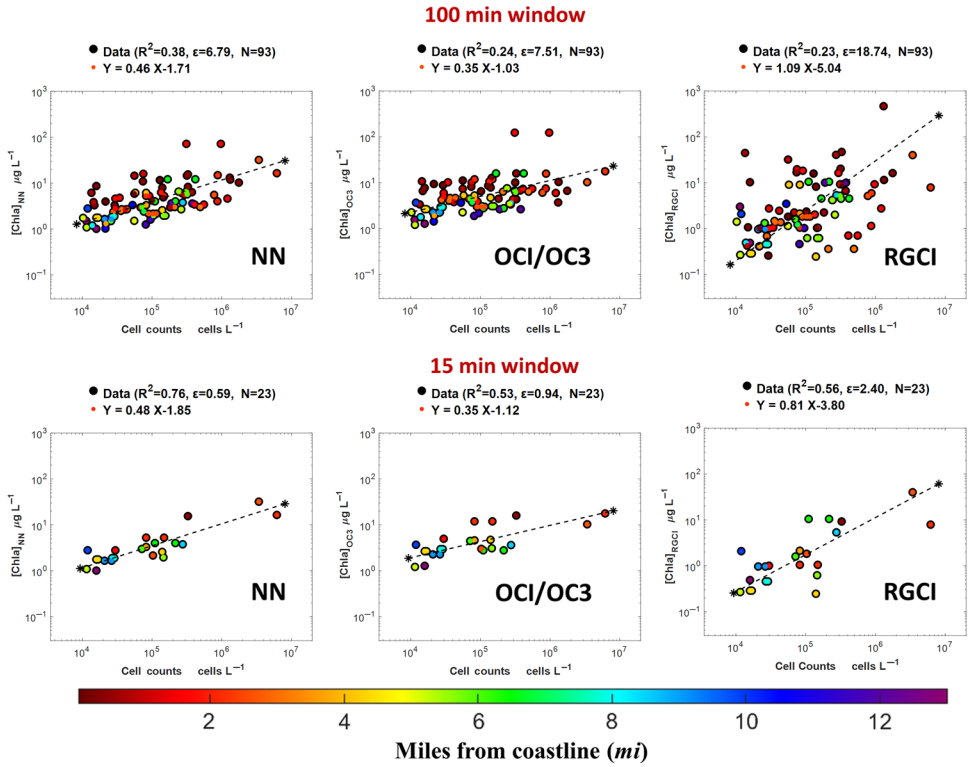

Fig. 7 *In situ* comparison for the available matchups points for 100- and 15-min overlap windows with *in situ* observations obtained using the different algorithms (NN, OCI/OC3, and RGCI). Color coding of the dots denotes distance to shore, with red being the closest.

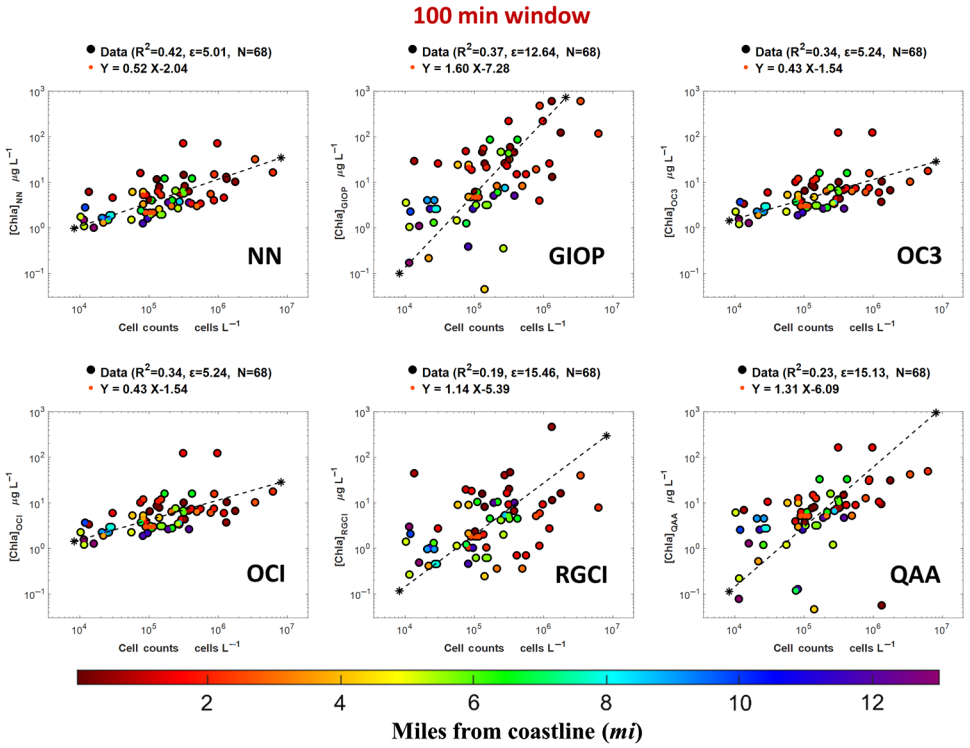

Fig. 8 Results for 68 *in situ* observations within 100 min of VIIRS overpass for the six algorithms showing retrieved [Chl*a*] against *KB* HABs cell counts for NN, GIOP, OC3, OCI, RGCI, and QAA retrievals. Color coding of the dots denotes distance to shore, with red being the closest.

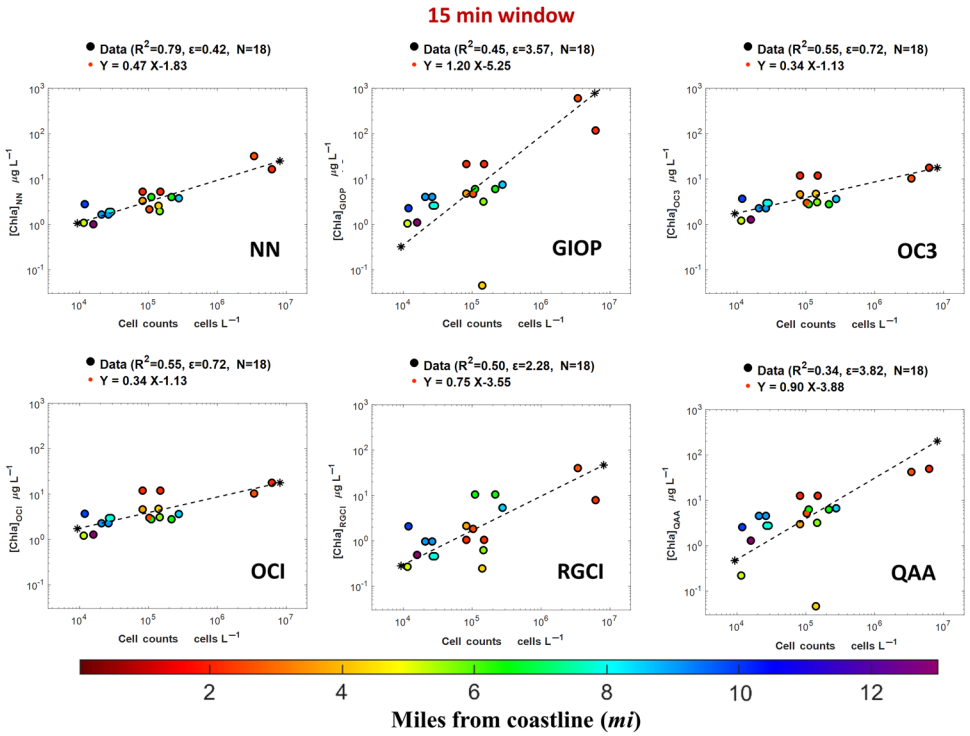

Fig. 9 Results for 18 *in situ* observations within 100 min of VIIRS overpass for the six algorithms showing retrieved [Chl*a*] against *KB* HABs cell counts for NN, GIOP, OC3, OCI, RGCI, and QAA retrievals. Color coding of the dots denotes distance to shore, with red being the closest.

Figure 7(b) shows that the results for 23 matchups observed when the observations window between overpass time and *in situ* measurements are restricted to 15 min, in which the impact of temporal variations is reduced. As can be seen, correlations and errors greatly improve for the 15-min window, compared to the 100-min window observations. It is also observed that NN retrievals exhibit the best performance for both time windows, in terms of both correlations and errors.

When VIIRS retrieval comparisons were extended to using GIOP and QAA algorithms, it was found that both algorithms exhibited negative values or no retrievals in many instances. When these negative values were excluded, there remained 68 valid matchups for the 100-min overpass window. The retrieved [Chl*a*] for these 68 matchups is shown against *in situ* cell counts in Fig. 8, for all retrieval techniques.

When the overlap observation window is reduced to 15 min, we have 18 valid matchups remaining, after excluding negative values associated with GIOP and QAA. Results for these 18 matchups are shown in Fig. 9. Again, as can be seen, correlations and errors greatly improve for the 15-min window over those for the 100-min window, Fig. 8.

Table 2 Statistics of comparison for Fig. 7.

y-axis [Chl*a*] ($\mu g\,L^{-1}$)	*x*-axis KB cell counts (cells L^{-1})	R^2	ε	Slope and intercept	*N*
NN	VIIRS 100-min window	0.38	6.79	$y = 0.46\,x - 1.71$	93
OC3		0.24	7.51	$y = 0.35\,x - 1.03$	93
OCI		0.24	7.51	$y = 0.35\,x - 1.03$	93
RGCI		0.23	18.74	$y = 1.09\,x - 5.04$	93
NN	VIIRS 15-min window	0.76	0.59	$y = 0.48\,x - 1.85$	23
OC3		0.53	0.94	$y = 0.35\,x - 1.12$	23
OCI		0.53	0.94	$y = 0.35\,x - 1.12$	23
RGCI		0.56	2.40	$y = 0.81\,x - 3.80$	23

Table 3 Statistics of comparison for Figs. 8 and 9.

y-axis [Chl*a*] ($\mu g\,L^{-1}$)	*x*-axis KB cell counts (cells L^{-1})	R^2	ε	Slope and intercept	*N*
NN	VIIRS 100-min window	0.42	5.01	$y = 0.52\,x - 2.04$	68
GIOP		0.37	12.64	$y = 1.60\,x - 7.28$	68
OC3		0.34	5.24	$y = 0.43\,x - 1.54$	68
OCI		0.34	5.24	$y = 0.43\,x - 1.54$	68
RGCI		0.19	15.46	$y = 1.14\,x - 5.39$	68
QAA		0.23	15.13	$y = 1.31\,x - 6.09$	68
NN	VIIRS 15-min window	0.79	0.42	$y = 0.47\,x - 1.83$	18
GIOP		0.45	3.57	$y = 1.20\,x - 5.25$	18
OC3		0.55	0.72	$y = 0.34\,x - 1.13$	18
OCI		0.55	0.72	$y = 0.34\,x - 1.13$	18
RGCI		0.50	2.28	$y = 0.75\,x - 3.55$	18
QAA		0.34	3.82	$y = 0.90\,x - 3.88$	18

The results in Figs. 8 and 9, which illustrate the impact of observation time windows on retrieval accuracies for all algorithms, are summarized in Tables 2 and 3. These results support the conclusion that, at least for these preliminary and somewhat limited data sets, the NN retrievals exhibit the best performances against the *in situ* measurements, for both the longer (100 min) and, more importantly, the shorter (15 min) overlap time windows. This was observed both in terms of higher correlations and lower errors against the *in situ* measurements.

3.4 *Assessing Validity of Filter Limits on Rrs551 and $a_{ph443} \geq 0.061\ m^{-3}$ (or [Chla]) in Context of Comparisons Against In Situ Measurements*

We also use the above matchups to assess the validity of the F1 and F2 filter limits (discussed in Sec. 3.1) for Rrs551 $\leq 6.0 \times 10^{-3}$ sr^{-1} and $a_{ph443} \geq 0.061$ m^{-3} or [Chl*a*]. Figure 10 shows the NN retrieved a_{ph443} matchups falling within the 15-min window, which were retrieved (without any filter constraints being applied for Rrs551 and [Chl*a*]). These show that there are three false negatives (marked with dark-gray arrows) and two false positives (marked with light-gray arrows) erroneously included within the Rrs551 and [Chl*a*] limiting values, out of 36 matchup points. It should be noted that the spatial variability within a pixel on the same day can be quite large and can include both extremely low and high *KB* cell concentrations.[1] This means that subpixel variability in the bloom concentration may be a key factor in creating apparent "false" positives. Planned future statistical analysis of false positives and negatives in retrieval results against *in situ* measurements is expected to result in further refinements of these limiting values and improvements in retrieval accuracies.

3.5 *Consecutive Satellite Images to Examine Temporal Changes*

From the results in Sec. 3.3, it was seen that reducing the time window between satellite and *in situ* observations can generally significantly increase the accuracy between VIIRS retrieved [Chl*a*] and *in situ* measured *KB* cell counts. These changes can be quite rapid.[65,66] To explore the potential for detecting HAB bloom changes over relatively short periods from overlapping consecutive satellite overpasses, we have also examined changes in three consecutive overlapping satellite images in Fig. 11. Two of these are from VIIRS, 96 min apart and an intermediate one is from MODIS-A, 70 min after the first VIIRS image.

We next examine NASA OC3 retrievals of [Chl*a*] for these three consecutive granules. Figs. 12(a)–12(c) show the retrieved NASA OC3 [Chl*a*] products from these consecutive VIIRS-MODIS-VIIRS images for the WFS near Sarasota, Florida, on 11/3/2014.

Since environmental factors, including wind direction and currents, are known to affect temporal changes, including down- and upwelling and transportation of *KB* blooms in the WFS,[47,65,67–69] we include wind information available for that date. Figure 13 shows data obtained from the National Data Buoy Center website for the C-MAN stations at Venice, Florida (Station VENF1). (27°4'21" N 82°27'10" W) showing the variability of the wind on 11/3/14 at the time of the VIIRS overpasses.

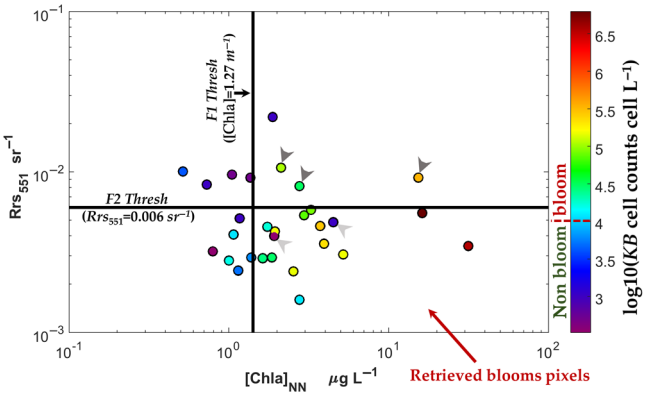

Fig. 10 The matchups falling within the 15-min window, with both filter thresholds.

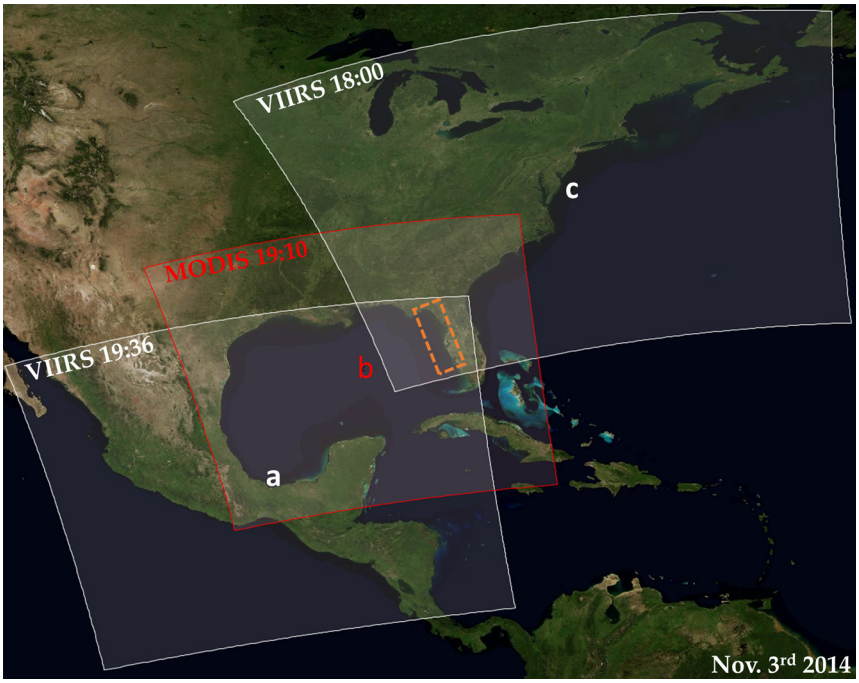

Fig. 11 The MODIS-A granule and two VIIRS granule within 100 min on November 3, 2014.

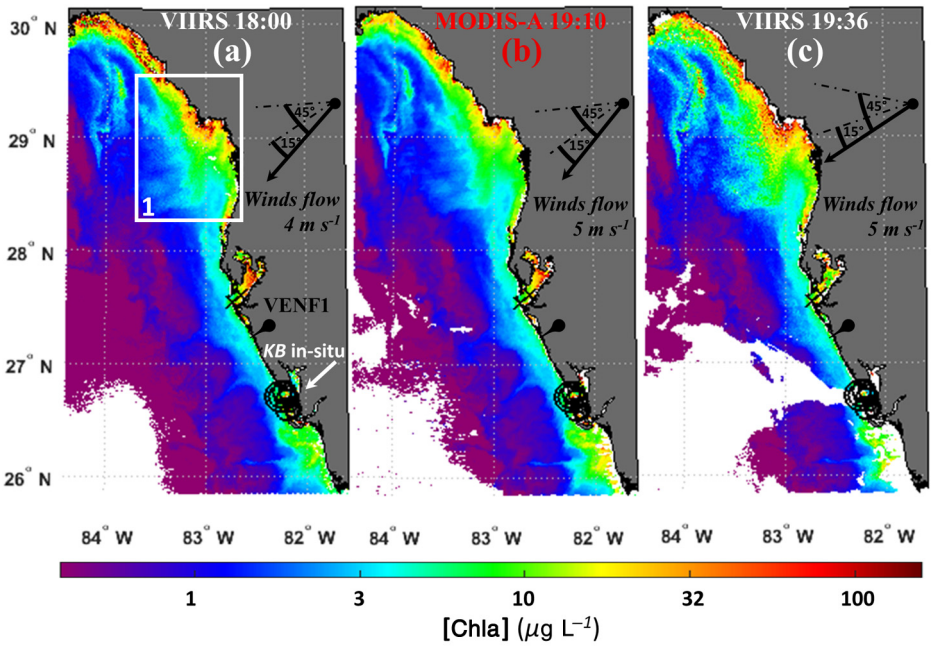

Fig. 12 (a)–(c) Changes in bloom for consecutive satellite images of region one.

It should be noted that in shallow waters, the angle between the wind-induced surface water movement and the wind direction can be as low as 15 deg (or even less depending on the wind velocity and water depth) rather than up to the 45-deg predicted by idealized spiral Ekman models for deeper waters.[70] We can probably assume that wind-induced current direction will be about 15-deg with the wind direction in the relatively shallow waters under consideration. This does not include tidal or other sources of current for which we have no information on that date. For qualitative comparison purposes, we show approximate wind directions and possible wind induced current directions (at 15 deg), overlaid in Fig. 12.

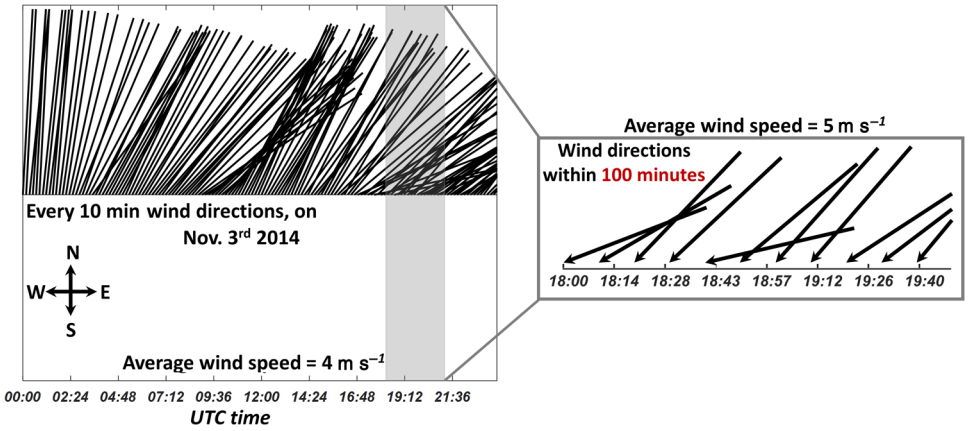

Fig. 13 Temporal changes in wind directions during November 3, 2014, obtained from VENF1 station (27°4'21" N 82°27'10" W). Zoomed image shows wind directions for the time period of the consecutive satellite images. The wind vectors were plotted in the direction toward which the wind is flowing.

We now examine in more detail region 1, in Fig. 12, and shown in the zoomed images in Fig. 14. The bloom, as delineated by the [Chl*a*] color contour in the images, appears, qualitatively, to increase in concentration and expand in the southwest direction over the 96-min interval between the consecutive overlapping VIIRS-MODIS-VIIRS images. These changes are reflected in the associated zoomed pixel images on the right-hand side of Fig. 14 and appear to provide qualitative visual indications of expansion of the bloom and its increasing [Chl*a*] concentration in the southwest direction. They also appear broadly consistent with the directions of wind and likely currents, though there is no specific or quantitative evidence of linkage. Furthermore, no movements of [Chl*a*] distribution patterns are discerned that would indicate transport. Nor is there evidence for identifying any specific causes for the changes observed, e.g., whether these are due to upwelling/downwelling effects or otherwise.

There is, also however, a caveat that might call into questions some of the above observations. We are aware of artifacts in the VIIRS retrieval imagery that tend to appear near the western edge of the image granule making it appear that [Chl*a*] concentrations are higher than the same values detected near the eastern edge. Under those circumstances, these artifacts could be playing a part in the apparent increase of the bloom in the consecutive VIIRS images in Figs. 12 and 14, which are from near the eastern and western edges of the consecutive VIIRS granules (Fig. 11). This possibility may be negated, however, by an examination of consecutive VIIRS retrievals in adjacent bloom free waters. These retrievals, which are found to be identical, are shown blue on the left-hand side of Fig. 14, for bloom free waters very closely adjacent to the blooms in region 1, and therefore, also near the eastern and western ends of the VIIRS image granules for the consecutive images. Thus, Fig. 14 (left-hand side) shows that, at least for these bloom free waters, VIIRS retrievals from both near granule edges are identical in the consecutive VIIRS images and are not affected by edge artifacts. Their validity is further confirmed by an identical MODIS-A retrieval, also in Fig. 14, whose image is not from a near granule edge. The fact that the two consecutive VIIRS retrievals are the same in bloom free waters and are unaffected by edge artifacts in turn supports the interpretation that the changes observed at the bloom/nonbloom boundaries (dotted rectangle) in consecutive images in Fig. 14(a) and 14(c) are not due to edge artifacts, but do in fact actually show expansion of the bloom into bloom free waters. This interpretation probably remains valid, even though near edge artifacts might still significantly impact the accuracies of changes in the higher bloom concentrations away from the bloom/nonbloom boundaries, such as those indicated by the color-coded concentrations in the zoomed images from the solid rectangle in Fig. 14 (and shown in right-hand side). These color-coded concentrations may, therefore, not be accurate because of near edge artifacts. In further support that it is changes that are being observed, it should be noted that these artifacts that may apply to retrievals because of western near edge effects in the VIIRS images would not apply to, or impact, the MODIS-A image, which is not at an edge, and which also shows similar expansion of the increasing [Chl*a*] bloom Fig. 14, region 1.

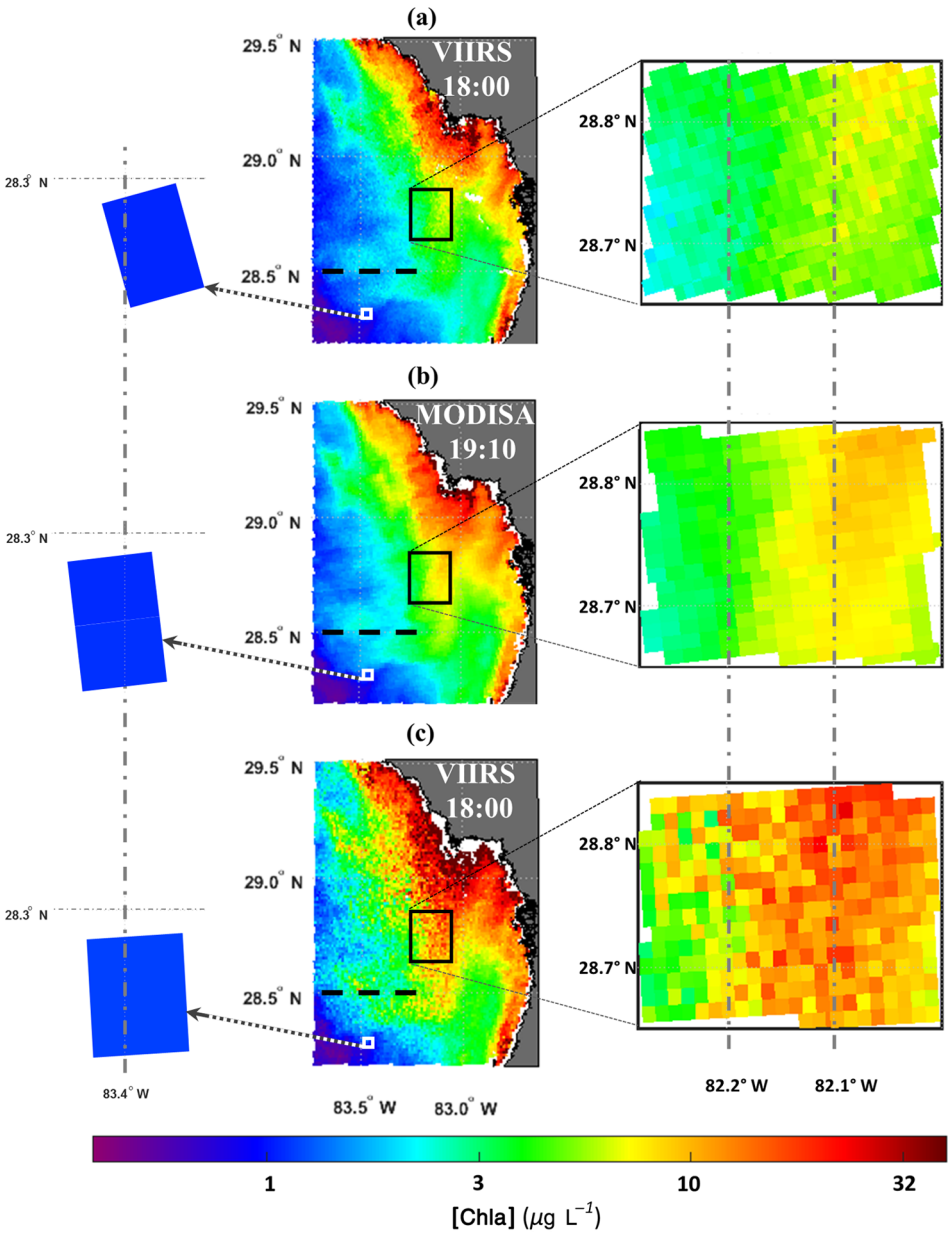

Fig. 14 Changes in bloom for consecutive satellite images of region 1 using retrieved OC3/OCI [Chl*a*].

For comparison with the VIIRS OC3 retrievals, in Figs. 12 and 14, which were discussed above, we show, in Fig. 15, retrievals using our NN technique for the same consecutive VIIRS observations. Results are qualitatively very similar to those from OC3, Fig. 14. Again, they also show bloom expansion to the southwest. NN retrieved [Chl*a*] values can be expected to differ in details from those of OC3, because of the different (higher) retrieval accuracies demonstrated by the NN technique (see Sec. 3.3). The zoomed features in Figs 15(a), 15(d), 15(e), and 15(h) show similarity with the equivalent OC3 retrievals in Fig. 14. Interestingly, we also observe essentially identical retrievals in the zoomed pixels of Figs. 15(b) and 15(f), which are from apparently unchanged high [Chl*a*] areas in Figs. 15(c) and 15(g), respectively. This might imply that the Rrs values at 486, 551, and 671 nm used as inputs into the NN are identical. Future matchups with *in situ* measurements may shed more light on these matters.

In the context of the above discussion, it is also worth reiterating that, as was noted previously in Sec. 2.2, all quality flags were applied for VIIRS and MODIS-A OC3/OCI ocean color level 2 information, as well as the Rrs values at 486, 551, and 671 nm for the NN retrievals, downloaded

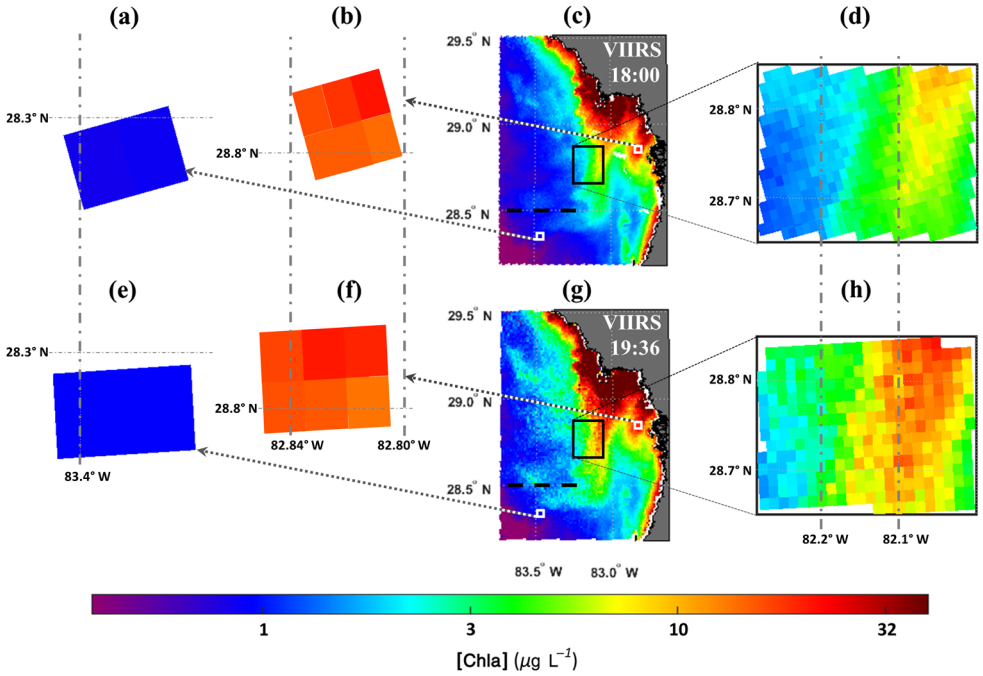

Fig. 15 Changes in bloom for consecutive VIIRS images of region 1 using NN retrieved [Chl*a*].

from NASA, which already has the appropriate corrections for both atmosphere and observation angle applied.[71] Water-leaving reflectances for our selected consecutive scenes are assumed to be independent of viewing geometries after BRDF/Albedo and atmospheric corrections are made. We would also note that the viewing angles for the consecutive VIIRS images are close, <5 deg (θ_{viirs_1} to θ_{viirs_2}. Furthermore, even if no correction was made for the ~60 deg observation angles (less than that, for the critical western near edge involved in the above images), potential errors would be relatively small,[72–74] (~1%) and would have no discernable impact on our qualitative interpretations that [Chl*a*] changes are observed in the retrieved images, while at the same time, not saying anything with regard to absolute magnitudes or accuracies.

In conclusion for this section on consecutive satellite images, it is recognized that additional studies that include comparisons from consecutive VIIRS retrievals of Rrs values, as well as comparisons of [Chl*a*] retrievals against simultaneous *in situ* measurements, would be needed to clarify the nature and magnitude of the changes being observed. However, given the difficulty of carrying out comprehensive calibration measurements of this type, we believe that it is reasonable to conclude that while consecutive overlapping satellite images can provide some evidence of temporal changes in *KB* HABs concentration in the WFS, they are unlikely to provide accurate or reliably useful information on the absolute magnitudes involved.

It should also be noted that while consecutive overlapping images appear to show temporal changes, there is insufficient evidence from them to attribute the relative contributions of drift, patchiness, upwelling/downwelling, or a combination of any of these to the causes of the changes. Section 3.6 presents the results of recent field measurements of *KB* HABs in the WFS, which much more solidly confirm *KB* HABs temporal variabilities as well as patchiness. They also support conclusions that the significantly improved retrieval accuracies that are obtained with shorter overlap time windows between satellite retrievals and *in situ* measurements (Sec. 3.3) reflect the impact of temporal variabilities.

3.6 *Field Measurements*

The evidence for temporal changes, intrapixel variations, and patchiness associated with blooms in the WFS is further supported more definitively by recent field measurements made in conjunction with Mote Marine Laboratories on 1/19/2017 off Lido Key, near Sarasota, Florida. Figure 16 shows the transect of measurements made. Several of these measurements were made at stations subpixel distances apart (generally 300 m) on an outward leg and were

Fig. 16 Transect of outward and return legs of field measurements.

then repeated for the same stations, matched as closely as possible with a GPS, on a return leg. Samples were taken at a 0.5-m depth and cell concentrations obtained by analysis at Mote Marine Laboratories.

The values shown in Fig. 17 give the *KB* cell counts at the different stations and the times of measurement. These are color coded, so that the same row color indicates the results for the same station on both the outward and return leg. It should be noted that, as might be expected with these high cell counts, the latter showed an excellent match with simultaneous collocated high performance liquid chromatography (HPLC), [Chl*a*] measurements. From Fig. 17, it can be seen that the changes in values at the same station generally increase with the time interval (between outward and return legs). Thus, the greatest change is for Station CV1701/CV1713 from 7.52×10^6 to 1.552×10^6 cells L^{-1} over the 120-min time interval between the two measurements. The second greatest change is that for the next station, CV1702/CV1712, where the change is from 1.776×10^6 to 1.326×10^6 cells L^{-1} for the 87-min time interval.

For the shortest time between measurements, CV1706/CV1708 the change is 0.952 to 0.690×10^6 cells L^{-1} over the 21-min interval between measurements. [It should also be noted that there is also a slight discrepancy in station positions recorded due to drift from measurement start (with GPS initial colocation) to completion and recording.]

Station	Depth (m^{-1})	Lat. (deg)	Long. (deg)	Start time (GMT)	End time (GMT)	*K. brevis* (cells L^{-1})	Time diff (min)
CV1701	0.7	27.31836	–82.59587	17:20	17:25	7,280,000	120
CV1713	0.7	27.31713	–82.59606	19:21	19:25	1,552,000	
CV1702	0.7	27.31500	–82.59831	17:48	17:52	1,776,000	87
CV1712	0.7	27.31480	–82.59846	19:15	19:19	1,326,000	
CV1703	0.7	27.31467	–82.60061	18:00	18:04	1,024,000	68
CV1711	0.7	27.31408	–82.60059	19:09	19:12	1,110,000	
CV1704	0.7	27.31296	–82.60277	18:07	18:12	964,000	54
CV1710	0.7	27.31289	–82.60298	19:03	19:06	590,000	
CV1705	0.7	27.31077	–82.60677	18:18	18:22	642,000	37
CV1709	0.7	27.31085	–82.60664	18:55	18:59	576,000	
CV1706	0.7	27.30681	–82.61356	18:27	18:32	952,000	21
CV1708	0.7	27.30686	–82.61364	18:48	18:51	690,000	

Fig. 17 Results of field measurements on 1/19/2017.

These results illustrate both the intrapixel variations that can typically occur (as well as inter pixel variations) and also confirm the temporal variations that can be expected. The relative contributions of drift or upwelling/downwelling to the results are not known.

In general, the consecutive satellite images and the field measurement observations lend support to our underlying thesis that the significantly increased bloom retrieval accuracy that occurs by shortening of the overlap time window between observation and *in situ* measurement matchups from 100 to 15 min is due to temporal changes in the observed bloom. They also serve to underline that derived magnitudes from satellite observations may be valid only for brief periods. To deal with these uncertainties, we are currently examining temporal and spatial averaging possibilities.

4 Summary and Conclusions

In the work reported here, NN algorithms using Rrs values from the 486-, 551-, and 671-nm VIIRS bands are used to retrieve an image of a_{ph443} values in the WFS. Then, these additional limiting constraints are applied, in two filter processes, F1 and F2 to eliminate from that image all a_{ph443} pixels that are not compatible with the existence of *KB* HABs. The residual image then shows only retrieved a_{ph443} values and their equivalent [Chl*a*] values that are consistent with the existence of *KB* HABs. This procedure was then used to retrieve *KB* HABs in the WFS. The efficacy of these NN retrievals was evaluated by comparison of retrieval accuracies obtained against simultaneous colocated *in situ* measurements.

For meaningful quantitative comparisons, it is important to have many data points. Accordingly, we sought all available matchups between VIIRS NN a_{ph443} (and equivalent [Chl*a*] retrievals) and *in situ KB* cell count measurements for the period 2012 to 2016 for which there was available VIIRS data. These comparisons showed that for VIIRS observations, the NN technique appeared to offer good potential for effective retrievals of *KB* HABs cell counts in the WFS. More specifically, these comparisons showed that when the overlap time window between *in situ* observations and satellite overpass measurements was reduced from 100 to 15 min, retrieval accuracies greatly improved and showed increased correlations and reduced errors. The comparisons against *in situ* matchups were also carried out for VIIRS retrievals using other algorithms: OCI/OC3, GIOP, QAA, and RGCI.

It was seen that for the available and somewhat limited data sets, the NN retrievals exhibited the best retrieval accuracies, among the techniques tested, against the *in situ* measurement data, for both the longer (100 min) and, more importantly, the shorter (15 min) overlap time windows. This was observed both in terms of higher correlations and lower errors against the *in situ* measurements. The results confirm the potential efficacy for detecting and quantifying *KB* HABs in the WFS using the NN technique.

Finally, consecutive satellite images qualitatively illustrated the temporal changes that can be associated with *KB* HABs in the WFS. The evidence for temporal changes was even more strongly complemented by recent field measurements off Sarasota, Florida, that quantitatively confirm the temporal changes and patchiness observed with *KB* HABs in the WFS.

Acknowledgments

This work was partially supported by grants from National Oceanographic and Atmospheric Administration (NOAA) through NOAA CREST, and NOAA JPSS, as well as the NASA Public Health and Air Quality Program (NRA: NN13ZDA001N). We would like to thank the NASA Ocean Color Processing Group for satellite imagery. We also thank NOAA HABSOS and Florida Fish and Wildlife Conservation Commission's Fish and Wildlife Research Institute (FWRI) groups for making *in situ KB* data available to us. The authors declare no conflict of interest.

References

1. A. El-Habashi et al., "Satellite retrievals of Karenia brevis harmful algal blooms in the West Florida shelf using neural networks and comparisons with other techniques," *Remote Sens.* **8**(5), 377 (2016).

2. US Department of Commerce, National Oceanic and Atmospheric Administration, "Harmful algal blooms," NOAA's National Ocean Service, 16 November 2009, http://oceanservice.noaa.gov/hazards/hab (22 November 2016).
3. C. Hu et al., "Red tide detection and tracing using MODIS fluorescence data: a regional example in SW Florida coastal waters," *Remote Sens. Environ.* **97**(3), 311–321 (2005).
4. R. Amin et al., "MODIS and MERIS detection of dinoflagellates blooms using the RBD technique," *Proc. SPIE* **7473**, 747304 (2009).
5. R. Amin et al., "Novel optical techniques for detecting and classifying toxic dinoflagellate Karenia brevis blooms using satellite imagery," *Opt. Express* **17**(11), 9126–9144 (2009).
6. M. Tomlinson, T. Wynne, and R. Stumpf, "An evaluation of remote sensing techniques for enhanced detection of the toxic dinoflagellate, Karenia brevis," *Remote Sens. Environ.* **113**(3), 598–609 (2009).
7. G. A. Carvalho et al., "Satellite remote sensing of harmful algal blooms: a new multi-algorithm method for detecting the Florida red tide (Karenia brevis)," *Harmful Algae* **9**(5), 440–448 (2010).
8. G. A. Carvalho et al., "Long-term evaluation of three satellite ocean color algorithms for identifying harmful algal blooms (Karenia brevis) along the west coast of Florida: a matchup assessment," *Remote Sens. Environ.* **115**(1), 1–18 (2011).
9. I. M. Soto Ramos, "Harmful algal blooms of the West Florida shelf and Campeche bank: visualization and quantification using remote sensing methods," PhD Dissertation, University of South Florida College of Marine Science (2013).
10. D. Blondeau-Patissier et al., "A review of ocean color remote sensing methods and statistical techniques for the detection, mapping and analysis of phytoplankton blooms in coastal and open oceans," *Prog. Oceanogr.* **123**, 123–144 (2014).
11. C. Hu et al., "A harmful algal bloom of Karenia brevis in the Northeastern Gulf of Mexico as revealed by MODIS and VIIRS: a comparison," *Sensors* **15**(2), 2873–2887 (2015).
12. I. M. Soto et al., "Evaluation and optimization of remote sensing techniques for detection of Karenia brevis blooms on the West Florida shelf," *Remote Sens. Environ.* **170**, 239–254 (2015).
13. I. Ioannou et al., "Neural network approach to retrieve the inherent optical properties of the ocean from observations of MODIS," *Appl. Opt.* **50**(19), 3168–3186 (2011).
14. I. Ioannou et al., "Deriving ocean color products using neural networks," *Remote Sens. Environ.* **134**, 78–91 (2013).
15. I. Ioannou et al., "Remote estimation of in water constituents in coastal waters using neural networks," *Proc. SPIE* **9240**, 92400T (2014).
16. A. El-habashi and S. Ahmed, "Neural network algorithms for retrieval of harmful algal blooms in the West Florida shelf from VIIRS satellite observations and comparisons with other techniques, without the need for a fluorescence channel," *Proc. SPIE* **9638**, 96380B (2015).
17. C. Le and C. Hu, "A hybrid approach to estimate chromophoric dissolved organic matter in turbid estuaries from satellite measurements: a case study for Tampa Bay," *Opt. Express* **21**(16), 18849–18871 (2013).
18. J. P. Cannizzaro et al., "A novel technique for detection of the toxic dinoflagellate, Karenia brevis, in the Gulf of Mexico from remotely sensed ocean color data," *Cont. Shelf Res.* **28**(1), 137–158 (2008).
19. J. P. Cannizzaro et al., "Detection of Karenia brevis blooms on the West Florida shelf using in situ backscattering and fluorescence data," *Harmful Algae* **8**(6), 898–909 (2009).
20. P. J. Werdell and S. W. Bailey, "An improved in-situ bio-optical data set for ocean color algorithm development and satellite data product validation," *Remote Sens. Environ.* **98**(1), 122–140 (2005).
21. IOCCG, "International ocean-colour coordinating group," June 2003, http://www.ioccg.org/groups/lee_data.pdf (9 March 2015).
22. A. Morel, "Optical properties of pure water and pure sea water," *Opt. Aspects Oceanogr.* **1**, 1–24 (1974).
23. H. R. Gordon et al., "A semianalytic radiance model of ocean color," *J. Geophys. Res.: Atmos.* **93**(D9), 10909–10924 (1988).

24. A. Morel, "Optical modeling of the upper ocean in relation to its biogenous matter content (Case I waters)," *J. Geophys. Res.* **93**(10), 10749–10768 (1988).
25. C. D. Mobley, *Light and Water: Radiative Transfer in Natural Waters*, Academic Press, San Diego, California (1994).
26. A. Bricaud et al., "Variability in the chlorophyll-specific absorption coefficients of natural phytoplankton: analysis and parameterization," *J. Geophys. Res.: Oceans* **100**(C7), 13321–13332 (1995).
27. R. P. Bukata et al., *Optical Properties and Remote Sensing of Inland and Coastal Waters*, CRC Press, Boca Raton, Florida (1995).
28. R. M. Pope and E. S. Fry, "Absorption spectrum (380-700 nm) of pure water. II. Integrating cavity measurements," *Appl. Opt.* **36**(33), 8710–8723 (1997).
29. A. Morel and S. Maritorena, "Bio-optical properties of oceanic waters-a reappraisal," *J. Geophys. Res.* **106**(C4), 7163–7180 (2001).
30. D. Stramski, A. Bricaud, and A. Morel, "Modeling the inherent optical properties of the ocean based on the detailed composition of the planktonic community," *Appl. Opt.* **40**(18), 2929–2945 (2001).
31. A. M. Ciotti, M. R. Lewis, and J. J. Cullen, "Assessment of the relationships between dominant cell size in natural phytoplankton communities and the spectral shape of the absorption coefficient," *Limnol. Oceanogr.* **47**(2), 404–417 (2002).
32. Z. Lee, K. L. Carder, and R. A. Arnone, "Deriving inherent optical properties from water color: a multiband quasi-analytical algorithm for optically deep waters," *Appl. Opt.* **41**(27), 5755–5772 (2002).
33. M. Babin et al., "Variations in the light absorption coefficients of phytoplankton, nonalgal particles, and dissolved organic matter in coastal waters around Europe," *J. Geophys. Res.: Oceans* **108**(C7), 3211 (2003).
34. Z. Lee, "Reports of the international ocean-colour coordinating group: fundamentals, tests of algorithms, and applications," IOCCG Report 5, Dartmouth, Canada (2006).
35. C. D. Mobley and L. K. Sundman, *Hydrolight 4.2 Technical Documentation*, p. 84, Sequoia Scientific, Incorporated, Redmond, Washington (2001).
36. F. Aires et al., "A new neural network approach including first-guess for retrieval of atmospheric water vapor, cloud liquid water path, surface temperature and emissivities over land from satellite microwave observations," *J. Geophys. Res. Atmos.* **106**(D14), 14887–14907 (2001).
37. F. Aires, C. Prigent, and W. B. Rossow, "Neural network uncertainty assessment using Bayesian statistics: a remote sensing application," *Neural Comput.* **16**(11), 2415–2458 (2004).
38. NASA's OceanColor Web by the Ocean Biology Processing Group (OBPG) at NASA's Goddard Space Flight Center, "Chlorophyll-a algorithm," https://oceancolor.gsfc.nasa.gov/PRODUCTS (22 November 2016).
39. NOAA Harmful Algal Blooms Observing System, "HABSOS," (15 July 2012), https://habsos.noaa.gov/ (22 November 2016).
40. J. O'Reilley et al., *SeaWiFS Postlaunch Calibration and Validation Analyses, Part 3*, S. B. Hooker and E. R. Firestone, Eds., p. 49, NASA Goddard Space Flight Center, Hampton, Virginia (2000).
41. J. E. O'Reilly et al., "Ocean color chlorophyll algorithms for SeaWiFS," *J. Geophys. Res.: Oceans* **103**(C11), 24937–24953 (1998).
42. C. Hu, Z. Lee, and B. Franz, "Chlorophyll a algorithms for oligotrophic oceans: a novel approach based on three-band reflectance difference," *J. Geophys. Res.: Oceans* **117**(C1), 73 (2012).
43. NASA's OceanColor Web by the Ocean Biology Processing Group (OBPG) at NASA's Goddard Space Flight Center, "Chlorophyll-a algorithm," https://oceancolor.gsfc.nasa.gov/atbd/chlor_a/ (22 November 2016).
44. K. Carder and R. Steward, "A remote-sensing reflectance model of a red-tide dinoflagellate off West Florida," *Limnol. Oceanogr.* **30**(2), 286–298 (1985).
45. R. P. Stumpf, "Applications of satellite ocean color sensors for monitoring and predicting harmful algal blooms," *Hum. Ecol. Risk Assess.: Int. J.* **7**(5), 1363–1368 (2001).

46. K. L. Mahoney, "Backscattering of light by Karenia brevis and implications for optical detection and monitoring," PhD dissertation, Univ. of South Mississippi, Stennis Space Center, p. 116 (2003).
47. R. Stumpf et al., "Monitoring Karenia brevis blooms in the Gulf of Mexico using satellite ocean color imagery and other data," *Harmful Algae* **2**(2), 147–160 (2003).
48. M. C. Tomlinson et al., "Evaluation of the use of SeaWiFS imagery for detecting Karenia brevis harmful algal blooms in the eastern Gulf of Mexico," *Remote Sens. Environ.* **91**(3), 293–303 (2004).
49. R. Stumpf and M. Tomlinson, "Remote sensing of harmful algal blooms," in *Remote Sensing of Coastal Aquatic Environments: Technologies, Techniques and Applications*, R. Miller, C. Del Castillo, and B. McKee, Eds., 277–292, Kluwer Academic Publishers, Springer, Dordrecht, The Netherlands (2005).
50. T. T. Wynne et al., "Detecting Karenia brevis blooms and algal resuspension in the western Gulf of Mexico with satellite ocean color imagery," *Harmful Algae* **4**(6), 992–1003 (2005).
51. S. E. Craig et al., "Use of hyperspectral remote sensing reflectance for detection and assessment of the harmful alga, Karenia brevis," *Appl. Opt.* **45**(21), 5414–5425 (2006).
52. P. A. Tester et al., "Relationships among water column toxins, cell abundance and chlorophyll concentrations during Karenia brevis blooms," *Cont. Shelf Res.* **28**(1), 59–72 (2008).
53. R. P. Stumpf et al., "Skill assessment for an operational algal bloom forecast system," *J. Mar. Syst.* **76**(1), 151–161 (2009).
54. L. Qi et al., "VIIRS observations of a Karenia brevis bloom in the northeastern Gulf of Mexico in the absence of a fluorescence band," *IEEE Geosci. Remote Sens. Lett.* **12**(11), 2213–2217 (2015).
55. R. M. Letelier and M. R. Abbott, "An analysis of chlorophyll fluorescence algorithms for the moderate resolution imaging spectrometer (MODIS)," *Remote Sens. Environ.* **58**(2), 215–223 (1996).
56. A. Gilerson et al., "Fluorescence component in the reflectance spectra from coastal waters. Dependence on water composition," *Opt. Express* **15**(24), 15702–15721 (2007).
57. M. J. Behrenfeld et al., "Satellite-detected fluorescence reveals global physiology of ocean phytoplankton," *Biogeosciences* **6**(5), 779–794 (2009).
58. J. Werdell, "Global bio-optical algorithms for ocean color satellite applications: inherent optical properties algorithm workshop at ocean optics XIX; Barga, Italy, 3-4 October 2008," *Eos, Trans. Am. Geophys. Union* **90**(1), 4 (2009).
59. P. J. Werdell et al., "Generalized ocean color inversion model for retrieving marine inherent optical properties," *Appl. Opt.* **52**(10), 2019–2037 (2013).
60. P. J. Werdell et al., "Retrieving marine inherent optical properties from satellites using temperature and salinity-dependent backscattering by seawater," *Opt. Express* **21**(26), 32611–32622 (2013).
61. Z. P. Lee, "QAA algorithm," 2002, http://ioccg.org/groups/Software_OCA/QAA_v5.pdf (22 November 2016).
62. Z. Lee and K. L. Carder, "Absorption spectrum of phytoplankton pigments derived from hyperspectral remote-sensing reflectance," *Remote Sens. Environ.* **89**(3), 361–368 (2004).
63. P. J. Franks, "Spatial patterns in dense algal blooms," *Limnol. Oceanogr.* **42**(5), 1297–1305 (1997).
64. L. Leng et al., "Ordinary least square regression, orthogonal regression, geometric mean regression and their applications in aerosol science," *J. Phys. Conf. Ser.* **78**, 012084 (2007).
65. R. Arnone et al., "Diurnal changes in ocean color in coastal waters," *Proc. SPIE* **9827**, 982711 (2016).
66. R. Arnone et al., "Ocean Weather—Interaction of physical and bio-optical processes across a river plume dominated shelf in the Gulf of Mexico," in *AGU Ocean Sciences*, New Orleans (2016).
67. P. A. Tester and K. A. Steidinger, "Gymnodinium breve red tide blooms: Initiation, transport, and consequences circulation," *Liminol. Oceanogr.* **42**, 1039–1051 (1997).
68. Y. Liu and R. H. Weisberg, "Patterns of ocean current variability on the West Florida shelf using the self-organizing map," *J. Geophys. Res.* **110**(C6) (2005).

69. Y. Liu and R. H. Weisberg, "Seasonal variability on the West Florida shelf," *Prog. Oceanogr.* **104**, 80–98 (2012).
70. NASA ocean motion and surface currents, "Ocean in motion: ekman transport background," http://oceanmotion.org/html/background/ocean-in-motion.htm (22 November 2016).
71. NASA's OceanColor Web by the Ocean Biology Processing Group (OBPG) at NASA's Goddard Space Flight Center, "Remote sensing reflectance (Rrs) algorithm," https://oceancolor.gsfc.nasa.gov/atbd/rrs/ (22 November 2016).
72. H. Yang and H. R. Gordon, "Remote sensing of ocean color: assessment of water-leaving radiance bidirectional effects on atmospheric diffuse transmittance," *Appl. Opt.* **36**(30), 7887–7897 (1997).
73. H. R. Gordon and B. A. Franz, "Remote sensing of ocean color: assessment of the water-leaving radiance bidirectional effects on the atmospheric diffuse transmittance for SeaWiFS and MODIS intercomparisons," *Remote Sens. Environ.* **112**(5), 2677–2685 (2008).
74. C. D. Mobley et al., "Atmospheric correction for satellite ocean color radiometry," A Tutorial and Documentation of the Algorithms Used by the NASA Ocean Biology Processing Group (2016).

Ahmed El-Habashi is a PhD student in the Department of Electrical Engineering at the City College of New York. He is a NOAA CREST fellow. His research in the Optical Remote Sensing Laboratory (ORSL) focuses on the remote sensing of ocean color and the detection of harmful algal blooms (HABs), as well as on the polarization properties of oceanic coastal waters and their relationship to fluorescence.

Claudia M. Duran is an undergraduate student in the Department of Earth System Science and Engineering at the City College. Her research in the ORSL has focused on the evaluation of satellite ocean color remote sensing techniques to retrieve HABs.

Vincent Lovko received his bachelor's degree in environmental science and his PhD at the Virginia Institute of Marine Science, Gloucester, Virginia. He is a staff scientist and manages the Phytoplankton Ecology Research Program at the Mote Marine Laboratory in Sarasota, Florida. He leads Mote's red tide program which conducts red tide monitoring and research under contract with the state of Florida, providing data for state red tide status updates and other collaborative data products.

Michelle C. Tomlinson received her BS degree in marine science biology from Southampton College of Long Island University and her MS degree in oceanography from Old Dominion University. She is an oceanographer with the National Centers for Coastal Ocean Science, NOAA. Her research focuses on the application of satellite-derived ocean color to detect, monitor, and forecast the occurrence of HABs, leading to the development of HAB forecast systems in the Gulf of Mexico and Lake Erie.

Richard P. Stumpf received his BS degree in environmental sciences from the University of Virginia, and his MS and PhD degrees in marine studies from the University of Delaware. He is an oceanographer with the National Centers for Coastal Ocean Science, NOAA. He leads research focusing on the application of satellite-derived ocean color to detect, monitor, and forecast the occurrence of HABs which has led to the development of an HAB forecast systems in the Gulf of Mexico and Lake Erie.

Sam Ahmed received his BA and MA degrees in electrical engineering from Cambridge University and his PhD from the University College, London. As director of the ORSL at the City College, New York, he has been involved in atmospheric LIDAR remote sensing of the atmosphere and in satellite remote sensing of ocean color.